

1-16-2012

The Mechanical Properties of Epoxy Composites Filled with Rubbery Copolymer Grafted SiO₂

Jianing Gao
Rensselaer Polytechnic Institute

Junting Li
University of South Carolina - Columbia, li.jt@mail.chem.sc.edu

Brian C. Benicewicz
University of South Carolina - Columbia, benice@sc.edu

Su Zhao
ABB Corporate Research

Henrik Hillborg
ABB Corporate Research

See next page for additional authors

Follow this and additional works at: https://scholarcommons.sc.edu/chem_facpub

 Part of the [Biochemistry Commons](#), and the [Chemistry Commons](#)

Publication Info

Published in *Polymers*, Volume 4, Issue 1, 2012, pages 187-210.

© Polymers 2012, the authors; licensee MDPI, Basel, Switzerland.

This article is an open access article distributed under the terms and conditions of the [Creative Commons Attribution license](#).

This Article is brought to you by the Chemistry and Biochemistry, Department of at Scholar Commons. It has been accepted for inclusion in Faculty Publications by an authorized administrator of Scholar Commons. For more information, please contact dillarda@mailbox.sc.edu.

Author(s)

Jianing Gao, Junting Li, Brian C. Benicewicz, Su Zhao, Henrik Hillborg, and Linda S. Schadler

Article

The Mechanical Properties of Epoxy Composites Filled with Rubbery Copolymer Grafted SiO₂

Jianing Gao ^{1,*}, Juntong Li ², Brian C. Benicewicz ², Su Zhao ³, Henrik Hillborg ³ and Linda S. Schadler ¹

¹ Department of Materials Science & Engineering, Rensselaer Polytechnic Institute, 110 8th Street, Troy, NY 12180, USA; E-Mail: schadl@rpi.edu

² Department of Chemistry and Biochemistry, University of South Carolina, Columbia, SC 29208, USA; E-Mails: li.jt@mail.chem.sc.edu (J.L.); benice@sc.edu (B.C.B.)

³ ABB Corporate Research, Forskargränd 7, 72226 Västerås, Sweden; E-Mails: su.zhao@se.abb.com (S.Z.); henrik.hillborg@se.abb.com (H.H.)

* Author to whom correspondence should be addressed; E-Mail: gaoj2@rpi.edu; Tel.: +1-518-276-3011; Fax: +1-518-276-6540.

Received: 17 December 2011; in revised form: 5 January 2012 / Accepted: 6 January 2012 /

Published: 16 January 2012

Abstract: This study demonstrated a method for toughening a highly crosslinked anhydride cured DGEBA epoxy using rubbery block copolymer grafted SiO₂ nanoparticles. The particles were synthesized by a sequential reversible addition-fragmentation chain transfer (RAFT) polymerization. The inner rubbery block poly(n-hexyl methacrylate) (PHMA) had a glass transition temperature below room temperature. The outer block poly(glycidyl methacrylate) (PGMA) was matrix compatible. A rubbery interlayer thickness of 100% and 200% of the particle core radius was achieved by grafting a 20 kg/mol and a 40 kg/mol PHMA at a graft density of 0.7 chains/nm² from the SiO₂ surface. The 20 kg/mol rubbery interlayer transferred load more efficiently to the SiO₂ cores than the 40 kg/mol rubbery interlayer and maintained the epoxy modulus up to a loading of 10 vol% of the rubbery interlayer. Both systems enabled cavitation or plastic dilatation. Improvement of the strain-to-break and the tensile toughness was found in both systems. We hypothesize that plastic void growth in the matrix is the primary mechanism causing the improvement of the ductility.

Keywords: toughened epoxy; rubbery interlayer; nanocomposites; RAFT polymerization

1. Introduction

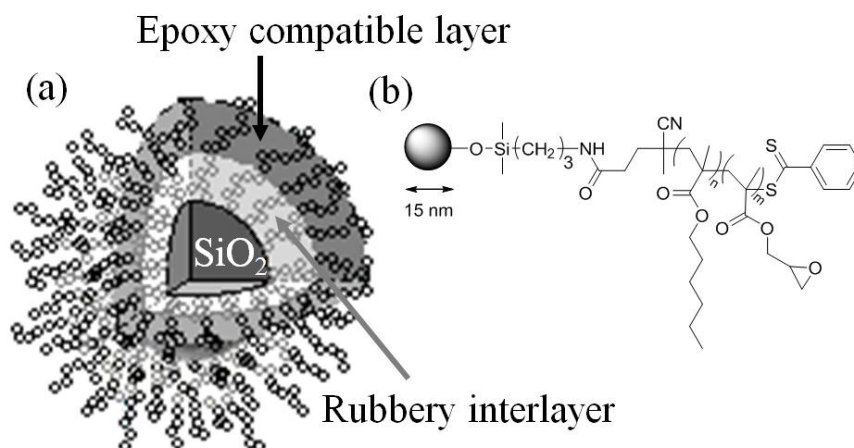
Epoxyes are widely used in industry. However, many epoxyes are brittle and have poor fracture toughness, weak impact strength and low resistance to fatigue crack propagation [1]. Epoxyes can be toughened by adding rubbery fillers, such as liquid rubbers [2–4] and preformed core/shell rubber particles [5–8]. Rubber cavitation happens under local hydrostatic stress. The cavitation releases the local hydrostatic stresses and causes plastic void growth and shear banding in the matrix. However, the addition of rubbers decreases the modulus, strength and glass transition temperature of epoxyes [9]. Rigid particles such as ceramic nanoparticles [10,11], clay [12], carbon nanotubes [13] and graphene [14], have also been found to toughen epoxyes by crack deflection, crack pinning, particle debonding, and plastic void growth, *etc.*, while increasing the modulus and strength and maintaining the glass transition temperature. However, they do not improve the matrix ductility and large volumetric loading of rigid fillers is required to improve the material toughness.

In order to combine the advantages of both rubbery and rigid fillers, Kinloch *et al.* [15] incorporated both SiO₂ nanoparticles and CTBN liquid rubber in an epoxy and found that the fracture energy increased synergistically with the use of both fillers. The modulus of the liquid rubber/epoxy composites was improved by adding SiO₂ nanoparticles up to 15.4 wt%. However, the modulus was still lower than the unmodified epoxy. The same modulus drop in the hybrid toughened epoxy was also observed by Liang and Pearson [16]. Lee and Yee [17] encapsulated micron sized glass beads with rubber at a ratio of rubber coating thickness to glass beads radius of less than 0.06. The tensile modulus of all coated glass bead filled epoxy composites was higher than the unmodified epoxy. However, the aggregation of particles during the encapsulating process, the poor bond between the rubber coating and the epoxy matrix, and the “thin” rubbery coating led to only a moderate toughening efficiency. This suggests that a strong matrix-rubber bond and good dispersion of the fillers are important. Recently, Zhao *et al.* [11] treated 50 nm Al₂O₃ nanoparticles with amino terminated tri-functional silane and found that 10 wt% of the silane treated Al₂O₃ significantly increased the ductility of the epoxy matrix with moderate improvement of the Young’s modulus. The paper suggests that the tri-functional silane generated a soft silane network around the nanoparticle cores, which played an important role in improving the matrix ductility and tensile toughness due to plastic void growth around the particles. However, no cavitation was found in the soft silane region and there was no increase in high strain rate fracture toughness. This suggests that the silane soft layer is beneficial in improving tensile toughness and ductility, but a thicker interlayer is needed to generate cavitation.

In this paper, we will explore the use of diblock copolymer modified SiO₂ nanoparticles in an epoxy. The grafted copolymer consists of a thick rubbery inner block (poly(*n*-hexylmethacrylate), PHMA) and a matrix compatible outer block (poly(glycidylmethacrylate), PGMA) with well-controlled molecular weight and graft density. This design aims at taking an advantage of a well bonded soft layer around the particle that can transfer tensile load to the silica core, maintaining the modulus and strength of the composites. Above a certain load, the rubbery layer will begin to fail, cavitating and

toughening the epoxy. The thickness of the rubbery interlayer needs to be controlled so it can be thin enough to effectively transfer load and thick enough to cause cavitation. The PGMA outer block was chosen to be matrix compatible, allowing the nanoparticles to be well dispersed. A generalized scheme of the rubbery copolymer grafted SiO_2 nanoparticles is shown in Figure 1(a).

Figure 1. A schematic of (a) a polymer grafted nanoparticle; and (b) the chemistry of the rubbery copolymer grafted nanoparticle.



2. Experimental Section

2.1. Materials

Huntsman Araldite[®] epoxy was used as the thermosetting matrix polymer. The system includes (i) Araldite F- bisphenol A liquid epoxy resin; (ii) HY905-modified dicarboxylic anhydride hardener; and (iii) DY062-amine catalyst. The SiO_2 nanoparticles were ORGANOSILICASOL[™] purchased from Nissan Chemical Co. Aminopropyldimethylethoxysilane (95%) was purchased from Gelest and used as received. Tetrahydrofuran (THF) (99.9%, Acros) was dried over CaH_2 overnight and distilled before use. 4-Cyanopentanoic acid dithiobenzoate (CPDB) was purchased from Strem Chemical Inc. and used as received. Both HMA and GMA were passed through a neutral alumina column to remove inhibitors before the polymerization. Unless otherwise specified, all chemicals were purchased from Fisher Scientific and used as received.

2.2. Composites Preparation and Characterization

The process of modifying the SiO_2 nanoparticles with chain transfer agents has been reported in the previous literature [17] and is briefly discussed here. SiO_2 nanoparticles (30 wt% in methyl isobutyl ketone) were diluted in dried THF, grafted with amino-functionalized silane coupling agents, and reacted with the chain transfer agents (activated CPDB) sequentially. UV-vis absorption spectra were acquired for graft density determination, and the nanoparticles were then dried and weighed.

The CTA anchored nanoparticles, monomer (HMA or GMA), AIBN and THF were added to a dried Schlenk tube. The mixture was degassed by three freeze-pump-thaw cycles, backfilled with nitrogen, and then placed in an oil bath at 60 °C for various intervals. The polymerization was quenched in ice

water. A sample of grafted chains was cleaved from the surface using hydrofluoric acid (HF). Typically, about 40 mg of nanoparticles was mixed with 4 mL of THF and 0.5 mL of HF, and the solution was allowed to stir at room temperature overnight, and then dried for GPC tests. If the polymers contained GMA residue, around 40 mg of nanoparticles were dissolved in 4 mL of methylene chloride, and then 4 mL of water, 0.5 mL of HF and one drop of Aliquot[®] 336 were added. After stirring overnight, the organic layer was taken out and evaporated for GPC tests. Molecular weights and molecular weight distributions (PDI) were determined by gel permeation chromatography conducted on a Varian 390-LC system equipped with refractive index, viscometry and light scattering detectors, and 3× PLgel 10 µm mixed-B LS columns (300 × 7.5 mm). THF was used as eluent and measurements were made at 30 °C and a flow rate of 1.0 mL/min. The GPC system was calibrated with poly (methyl methacrylate) standards obtained from Polymer Laboratories. The remainder of the particles were precipitated in methanol to remove unreacted monomers, and then either re-dispersed in THF to polymerize another block, or re-dispersed in methylene chloride.

The methylene chloride solution was then mixed with epoxy resin. The solvent in the mixture was evaporated until the mass of the mixture remained unchanged, indicating that all the solvent was gone. The hardener and the catalyst were then added to the particle-resin mixture and thoroughly mixed using a Hauschild Dual Asymmetric Centrifugal mixer. The mixture was cured at 80 °C for 10 hours and 135 °C for 10 h in a silicone mold. Nanocomposites with 0.1 vol%, 0.3 vol%, 0.6 vol% and 1 vol% SiO₂ cores were prepared. The dispersion was characterized using a DI-NanoScope III atomic force microscope (AFM) from Veeco. The curing process of the epoxy matrix was studied by an isoconversional method on a Modulated Differential Scanning Calorimeter (MDSC) model Q100 from TA Instruments. About 10 mg uncured sample was cured in closed aluminum pans in the MDSC at heating rates of 2.5, 5, 7.5, 10 and 12.5 °C/min. Activation energies were calculated according to the Kissinger equation. The glass transition temperatures of the nanocomposites were measured by DSC at a heating rate of 10 °C/min and dynamic mechanical analysis on a DMTA V from Rheometric Scientific from −150 to 200 °C at 2 °C/min.

2.3. Tensile Tests

Tensile tests were carried out using an Instron 4201 at room temperature and constant cross-head speed of 0.1 mm/min. Dog bone shaped specimens were made. Young's modulus, ultimate tensile stress and strain-to-break of epoxy and epoxy nanocomposites were measured. At least 5 composite samples were tested for each loading according to ASTM standard D638-08.

2.4. Fracture Analysis

The fracture surface of the neat epoxy and nanocomposites was analyzed by a JEOL 6330F field emission scanning electron microscope (SEM). The sub surface failure was characterized by a JOEL CM12 transmitted electron microscope (TEM) on the vertical plane beneath the fracture surface.

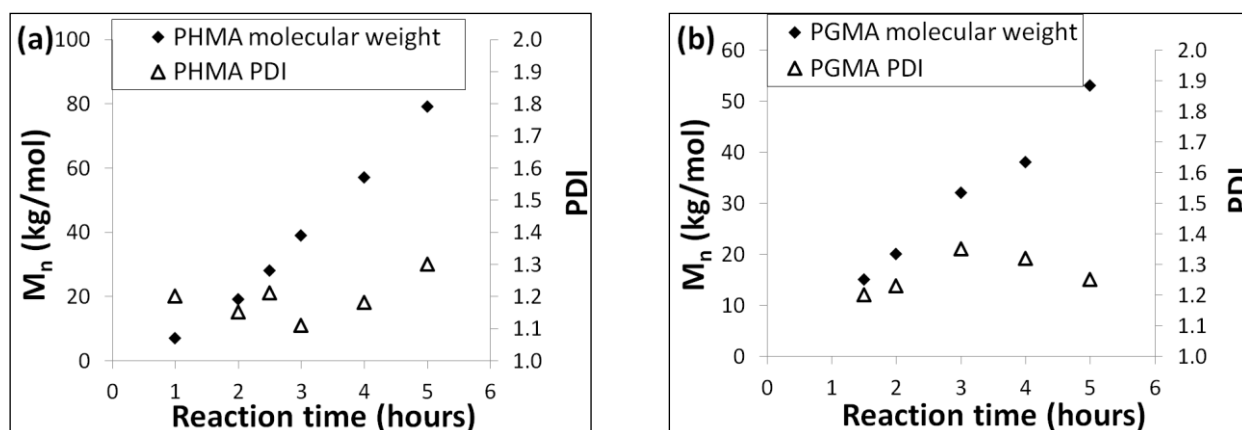
3. Results and Discussion

3.1. Synthesis

Block-copolymer grafted SiO_2 nanoparticles were synthesized by sequential reversible addition-fragmentation chain transfer (RAFT) polymerization from the surface of the nanoparticles [18]. RAFT provides quantitative control over the molecular weight and polydispersity (PDI) of each block. The graft density can be adjusted from approximately 0.01 chains/nm^2 to 0.7 chains/nm^2 [19]. To ensure that the epoxy compatible layer is compact enough to reduce the epoxy monomer penetration and shield the rubbery interlayer, nanoparticles with high graft density of 0.7 chains/nm^2 were prepared.

The polymerization of each monomer on SiO_2 nanoparticles was studied separately prior to block copolymer (PHMA-*b*-PGMA) synthesis. The results of the RAFT polymerization of HMA (hexylmethacrylate) and GMA (glycidylmethacrylate) are shown in Figure 2. This figure shows that the PHMA molecular weight increased almost linearly with the reaction time. However, the PDI of the PHMA did not vary significantly during the reaction process. The polymerization of GMA on the SiO_2 nanoparticles exhibited a similar linear relationship between molecular weight and reaction time with slightly higher PDI.

Figure 2. Plots showing the dependence of molecular weight and PDI on reaction time for the RAFT polymerization of HMA (a) and GMA (b) (5 M in THF) at 60°C with AIBN as initiator ($1.5 \times 10^{-5} \text{ M}$) mediated with RAFT agent anchored silica nanoparticles ($1.5 \times 10^{-4} \text{ M}$; 0.61 chains/nm^2). The gel permeation chromatography (GPC) system was calibrated with poly(methyl methacrylate) standards.



The rubbery block was synthesized at two molecular weights, 20 kg/mol and 40 kg/mol, to study the effect of the rubbery interlayer thickness on the mechanical properties of the copolymer grafted SiO_2 nanocomposites. To ensure good dispersion of the rubbery block grafted SiO_2 nanoparticles, a 20 kg/mol PGMA block was grown from the 20 kg/mol PHMA block. Similarly, a 40 kg/mol PGMA block was grown from the 40 kg/mol PHMA block. The nanocomposites are therefore denoted as 20k20k for the 20 kg/mol PHMA and 20 kg/mol PGMA grafted SiO_2 filled epoxy and 40k40k for the 40 kg/mol PHMA and 40 kg/mol PGMA grafted SiO_2 filled epoxy.

Good dispersion was achieved in both the 20k20k and the 40k40k systems as shown in the AFM images in Figure 3. To show that the PHMA is acting as a rubbery interlayer, AFM images were

taken comparing the PHMA-*b*-PGMA systems to silica nanoparticles with only PGMA attached. Nanocomposites with a loading of 0.3 vol% SiO₂ cores were used for AFM observation to ensure that the grafted particles were isolated. A sharp phase change between the SiO₂ cores and the epoxy matrix was observed in the solely PGMA grafted SiO₂ epoxy nanocomposites (see Figure 3(a,b)). When the PHMA is present, a softer interphase can be seen in both the 20k20k and the 40k40k systems (see Figure 3(c–f)). This softer interphase appears darker than the epoxy matrix in the phase images (see Figure 3(d,f)).

Figure 3. (a) AFM height image of 0.3 vol% PGMA-SiO₂/epoxy; (b) AFM phase image of 0.3 vol% PGMA-SiO₂/epoxy; (c) AFM height image of 0.3 vol% 20k20k-SiO₂/epoxy; (d) AFM phase image of 0.3 vol% 20k20k-SiO₂/epoxy; (e) AFM height image of 0.3 vol% 40k40k-SiO₂/epoxy; (f) AFM phase image of 0.3 vol% 40k40k-SiO₂/epoxy.

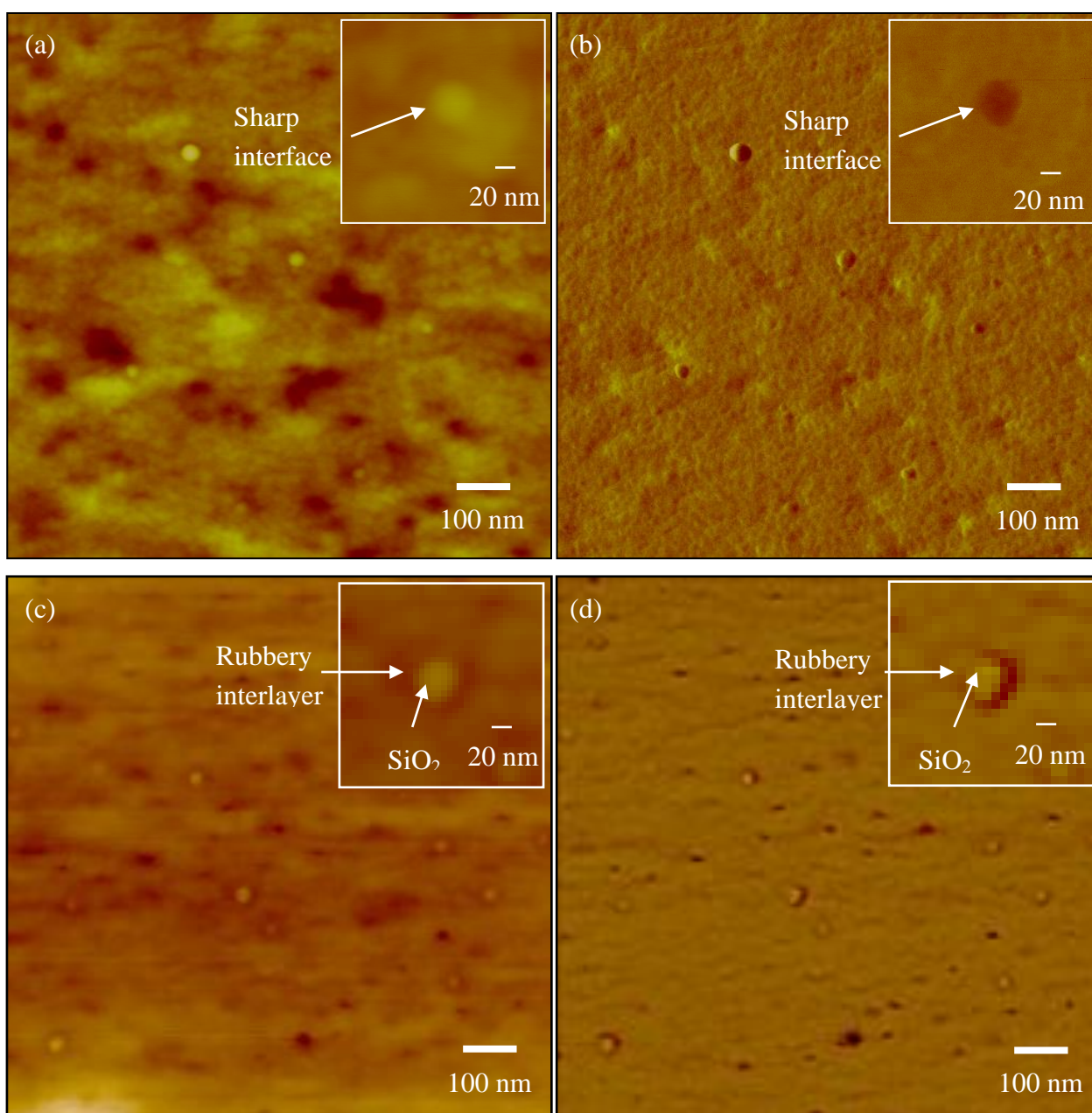
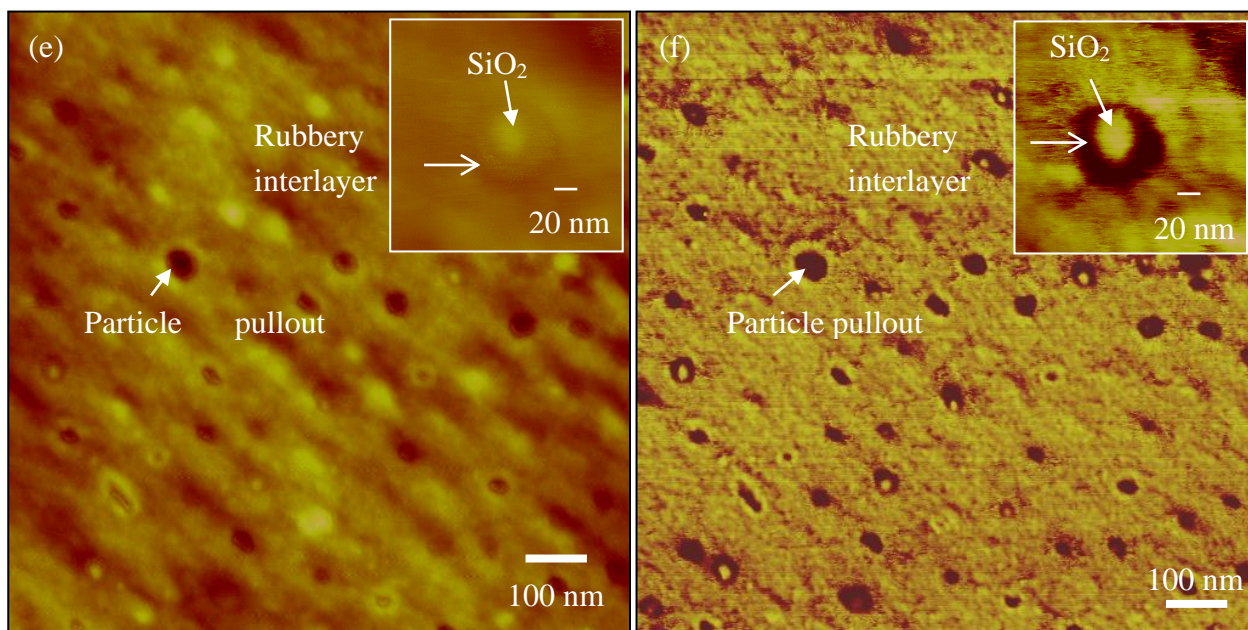
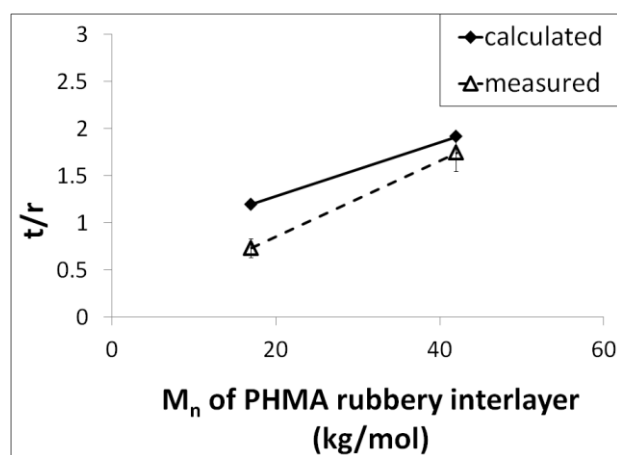


Figure 3. Cont.



The ratio of the rubbery interlayer thickness to the SiO_2 radius of the 20k20k and the 40k40k systems was analyzed based on at least 10 particles from each AFM image using an image processing program ImageJ [20]. The measured values were compared to the ratio calculated using the rubbery block molecular weight, graft density and bulk PHMA density of 1.0007 g/cm^3 . The comparison is summarized in Figure 4.

Figure 4. A comparison between the measured and calculated ratio of the rubbery interlayer thickness (t) and the radius (r) of the particle cores for particles with a 20 kg/mol and 40 kg/mol PHMA rubbery interlayer.



Both the calculated and the measured results showed that the rubbery interlayer thickness increases as expected with increasing molecular weight. The AFM images were taken using a tip with a radius of 7 nm. Because the tip radius was on the order of the radius of the particle, the apparent particle size in the AFM image is greater than the real particle size. This contributes to the discrepancy between the calculation and the measured interlayer thickness to particle radius ratio. Due to this limitation of the

AFM imaging, the calculated rubbery interlayer to particle core ratio was used when calculating the volume percent of the rubbery interlayer in the nanocomposites. The volumetric loading of the SiO₂ cores in the current paper, together with the volumetric ratio of the PHMA rubbery interlayer to the SiO₂ cores and the volumetric fraction of the SiO₂ cores in the polymer-SiO₂ nanoparticles are summarized in Table 1.

Table 1. Volumetric loading of the copolymer grafted SiO₂/epoxy nanocomposites prepared in the paper. The volume ratio of the PHMA rubbery interlayer to that of the SiO₂, and the volumetric fraction of the SiO₂ core in the polymer grafted SiO₂ nanoparticles for both 20k20k and 40k40k are also calculated and summarized.

Sample	t_{PHMA}/r_{SiO_2}	V_{PHMA}/V_{SiO_2}	$V_{SiO_2}/V_{polymer-SiO_2}$	Vol% of SiO ₂ Cores
20k20k	1	13.8	3.50%	0.1%
				0.3%
				0.6%
				1.0%
40k40k	2	34.2	1.44%	0.1%
				0.2%
				0.3%

3.2. Curing and Glass Transition Temperature

The PGMA outer block of the copolymer grafted SiO₂ nanoparticles introduces additional epoxy groups to the composite, which can influence the curing process of the matrix by decreasing the stoichiometric anhydride hardener to epoxy ratio. This can impact the glass transition temperature and the mechanical properties of the nanocomposites. The curing can be further complicated when one considers that the PGMA layer might scavenge epoxy and anhydride monomers (because the PGMA layer is epoxy compatible), probably at different efficiency. The difference in the curing process between the nanocomposites and the neat epoxy alone can impact the glass transition temperature and mechanical properties. However, we can still study the influence of the rubbery interlayer on the glass transition temperature and the mechanical properties of the nanocomposites by separating the effect of the interlayer from the influence of the anhydride/epoxy ratio. The impact of the anhydride to epoxy ratio on the glass transition temperature and the mechanical properties of the neat epoxy was studied. The curing of neat epoxy with an anhydride to epoxy ratio from 0.8 to 1.2 was analyzed using modulated differential scanning calorimetry. The influence of the ratio on the curing mechanism (evaluated by curing activation energy) and the degree of curing completion (indicated by glass transition temperature) was quantified. The activation energy for curing was calculated from the Kissinger equation [21–23],

$$\frac{d \left(\ln \frac{q}{T_{q,p}^2} \right)}{d \left(\frac{1}{T_{q,p}} \right)} = -\frac{E}{R} \quad (1)$$

where $T_{q,p}$ is the temperature at the heat flow peak generated by a heating rate of q . E is the activation energy of the curing reaction and R is the gas constant. The activation energy was measured from the

slope of $1/T_{q,p}^2$ vs. $\ln q/T_{q,p}^2$. Table 2 shows the average activation energy to cure the neat epoxy with an anhydride to epoxy ratio (denoted as R in Table 2) of 0.8, 1 and 1.2. The activation energy of the three systems was similar (within 0.2%). However, at a ratio of 1.2 there is a 7% decrease in the T_g from the 1:1 ratio. Therefore, changing the anhydride to epoxy ratio by 20% from the stoichiometric ratio does not change the curing mechanism, but does change the extent of curing completion.

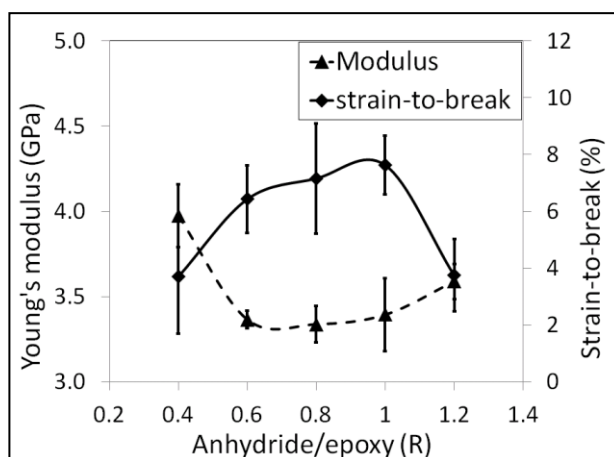
Table 2. The glass transition temperature of the epoxy systems.

Material	vol% of SiO ₂ Cores	R *	Activation Energy (J/g)	T _g (°C)
Neat epoxy		0.8	74.3	110
		1	75.8	112
		1.2	76.7	105
20k20k				
	0.1%	0.99		109
	0.3%	0.98		110
	0.6%	0.96		105
40k40k	1%	0.93		100
	0.1%	0.98		110
	0.2%	0.97		110
	0.3%	0.95		109

* R is the number ratio of anhydride reacting groups and epoxy groups from the epoxy resin and the PGMA epoxy compatible layer.

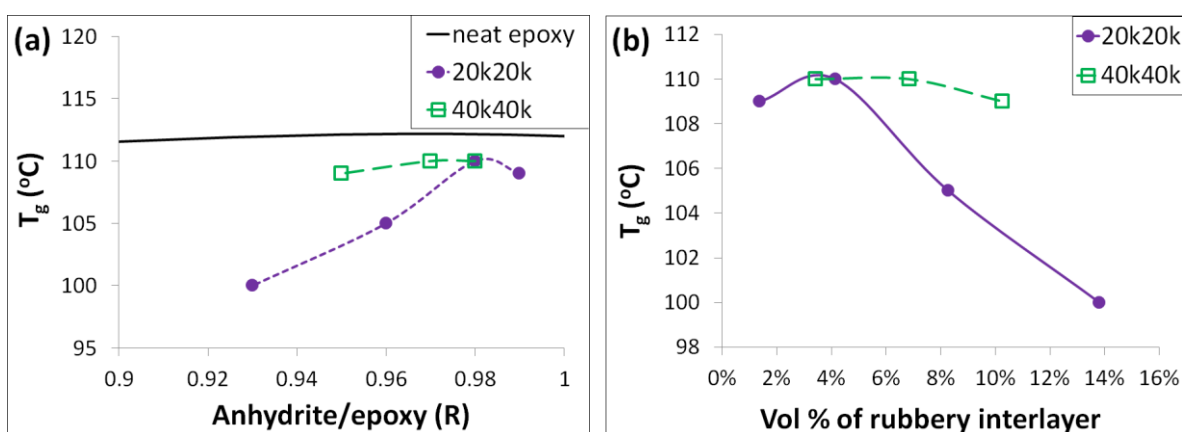
The impact of the anhydride to epoxy ratio on the mechanical properties of unfilled epoxy was also determined. Figure 5 shows the mechanical properties (Young's modulus and strain-to-break) of the neat epoxy with anhydride to epoxy ratio from 0.4 to 1.2. It is observed that the modulus and strain-to-break of the neat epoxy remain unchanged in the window of 0.8 to 1, suggesting that the mechanical properties of the epoxy matrix are insensitive to the degree of curing completion when the anhydride to epoxy ratio is between 0.8 and 1 in the current study. Similar results have been found for other anhydride cured epoxies [24].

Figure 5. Modulus and strain-to-break of the neat epoxy with different anhydride/resin ratios.



Because the glass transition temperature and the mechanical properties of the neat epoxy are not significantly altered for the anhydride to epoxy ratios from 0.8 to 1; the addition of the PGMA layer only alters the potential anhydride/epoxy ratio from 0.9 to 1 (also calculated in Table 2); and the amount of epoxy and anhydride monomer that penetrates the brush is unknown, the anhydride to epoxy ratio was not altered for the nanocomposites. Based on the study above, the impact of the grafted polymer on the glass transition temperature could be extracted from the difference between the relationship of the anhydride to epoxy ratio and the glass transition temperature of the nanocomposites (Figure 6(a)). It is interesting to note that the glass transition temperature of the composites is always lower than the neat epoxy, which is due to the existence of the grafted polymer. As shown in Figure 6(b), the 20k20k system exhibited a larger decrease in T_g at the same volumetric loading of the PHMA rubbery layer as the 40k40k composites. This suggests that the drop in T_g of the 20k20k composites is not due to the rubbery volume percent alone. The reason for this interesting phenomenon is unclear.

Figure 6. Plots of glass transition temperature vs. (a) anhydride/epoxy ratio R of different epoxy systems; (b) the rubbery interlayer volume percent in the 20k20k and the 40k40k systems.



3.3. Mechanical Properties of HMA-*b*-GMA-SiO₂/Epoxy Nanocomposites

To understand whether the rubbery interlayer thickness in the current study will alter the mechanical properties of the rubbery interlayer, temperature sweep dynamic mechanical analysis was performed on the neat epoxy, 0.3 vol% and 1 vol% 20k20k-SiO₂ and 0.3 vol% 40k40k-SiO₂/epoxy nanocomposites. The temperature sweep curves for all four systems are shown in Figure 7. There are two peaks in the loss modulus curve: the glass transition and β -transition for the unmodified epoxy. An additional peak was observed in the loss modulus curves of the 1 vol% 20k20k-SiO₂/epoxy around 0 °C. The β -transition broadens at around 0 °C for the 0.3 vol% 40k40k-SiO₂/epoxy. Neither a peak nor a broadening at 0 °C is obvious in the 0.3 vol% 20k20k-SiO₂. The peak around 0 °C is due to the existence of the rubbery interlayer, and matches the glass transition temperature of the PHMA, which has been reported to be around 0 °C [25,26]. A plot of the loss modulus increase at 0 °C vs. the volume percent of the rubbery interlayer is shown in Figure 8, showing that the increase in the loss modulus is almost linearly proportional to the volume percent of the rubbery interlayer. This data suggests that the dynamic mechanical properties of the PHMA interlayer are insensitive to the molecular weights that were studied in the paper.

Figure 7. A temperature sweep of the neat epoxy and PHMA-b-PGMA grafted SiO₂ epoxy nanocomposites. (a) Storage modulus vs. temperature; (b) Loss modulus vs. temperature.

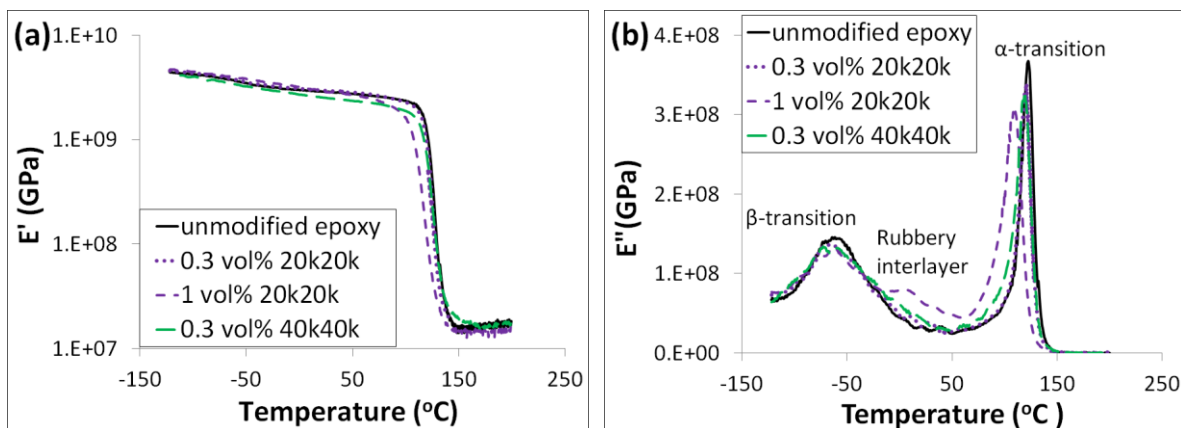
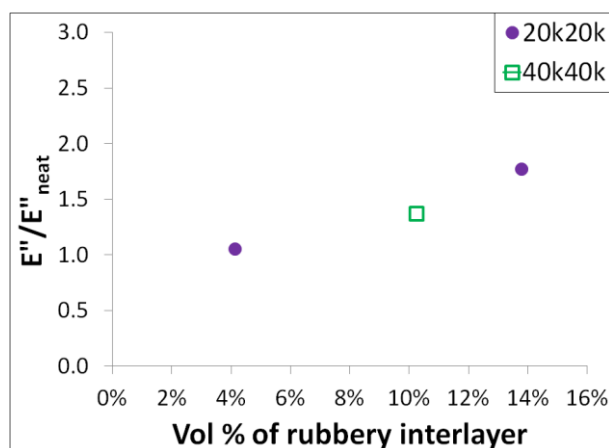


Figure 8. The rubbery interlayer volume fraction vs. the ratio of loss modulus of the nanocomposites and that of the neat epoxy at 0 °C.



Important information about the matrix molecular weight between crosslinks M_c and toughenability can be drawn from the DMA data. It is believed that lightly crosslinked epoxies ($M_c > 500$ g/mol) can be toughened more efficiently by rubbers than highly crosslinked epoxies ($M_c < 500$ g/mol). The toughening effect levels off as the molecular weight between crosslinks increases ($M_c > 3000$ g/mol) [27]. The M_c of the epoxy matrix can be calculated from the following equation based on the theory of rubber elasticity [28]:

$$M_c = \frac{\rho RT}{E_r} \quad (2)$$

where ρ is the density of an epoxy at temperature T , R is the gas constant and E_r is the storage modulus of the epoxy at 50 °C above its glass transition temperature. A comparison of the toughenability of the studied DGEBA/anhydride epoxy to that of a highly crosslinked and a lightly crosslinked epoxy from the literature is shown in Table 3. The fracture energy of the lightly crosslinked epoxy matrix with $M_c = 679$ g/mol improved by a factor of 3 with the addition of 5 wt% rubber, while at the same filler concentration the fracture energy increased by a factor of about 2.5 for the highly crosslinked epoxy matrix with $M_c = 260$ g/mol. The studied epoxy with $M_c = 312$ g/mol is a highly crosslinked epoxy with small toughenability.

Table 3. A comparison of the toughenability of the epoxy used in this study to some literature systems.

System	M_c (g/mol)	G_{1c} (J/m ²)	G_{1c} at 5 wt% Rubber (J/m ²)
DGEBA/anhydride (the system used in the current work)	312	281	
DGEBA+DDS [27]	260	150	400
DGEBA+DDS [27]	679	4500	14000

The tensile properties, including Young's modulus, tensile strength and strain-to-break of the neat epoxy, 20k20k-SiO₂, 40k40k-SiO₂ and untreated SiO₂ filled epoxy nanocomposites with different loadings are summarized in Table 4. The strain-to-break of the rubbery grafted SiO₂/epoxy nanocomposites increased with increasing loading. A *t*-test shows that the strain-to-break of the rubbery grafted SiO₂/epoxy nanocomposites is significantly larger than the neat epoxy at a confidence level of 95% (except at 0.1% SiO₂ core), while the strain-to-break of the bare SiO₂/epoxy nanocomposites showed no statistical difference from the neat epoxy. This suggests that the increase in the copolymer grafted SiO₂/epoxy nanocomposites was not due to the existence of the SiO₂ cores but the existence of the rubbery layer. Representative stress strain curves of all three composites studied are shown in Figure 9. Figure 10 shows the relationship between the rubbery interlayer volume percent and the mechanical properties of the nanocomposites. Both the 40k40k and 20k20k systems improve the strain-to-break and the tensile toughness with a similar trend (Figure 10(a)), with the 40k40k showing a better improvement below 8 vol% of the rubbery interlayer. However, an obvious decrease in the modulus and tensile strength in the 40k40k systems occurs at a lower rubbery interlayer volume fraction than in the 20k20k system (Figure 10(b)). Therefore, the 20k20k system can achieve similar improvement in ductility and tensile toughness of the matrix but maintain better modulus and tensile strength than the 40k40k system. It is thus possible that an improvement in the strain-to-break, while maintaining modulus and tensile strength, can be achieved by reducing the interlayer thickness and increasing the particle loading.

Table 4. The tensile properties of the nanocomposites and the neat epoxy. Error estimates are the measured standard deviations.

Sample	$f_{\text{silica cores}}$	ϵ_b (%)	(<i>t</i> -test)	UTS (MPa)	E (GPa)	Area under σ - ϵ Curve W (MPa or 10 ⁻⁶ J/m ³)
Neat		7.36 ± 0.41		83.73 ± 1.15	3.30 ± 0.07	5.3 ± 1.6
Bare- SiO ₂	0.3	6.99 ± 0.34	-	83.54 ± 0.34	3.40 ± 0.05	5.3 ± 0.4
	1.6	7.19 ± 0.96	9%	83.46 ± 1.10	3.43 ± 0.10	5.7 ± 1.0
	3	7.24 ± 1.74	19%	84.24 ± 0.94	3.67 ± 0.09	6.0 ± 0.9
20k20k-SiO ₂	0.1	7.18 ± 0.35	74%	82.35 ± 1.15	3.17 ± 0.09	5.6 ± 1.2
	0.3	9.49 ± 1.02	98%	79.60 ± 1.37	3.18 ± 0.08	6.1 ± 1.4
	0.6	9.07 ± 0.30	93%	75.72 ± 1.00	3.26 ± 0.13	5.8 ± 1.0
	1	11.52 ± 0.45	99%	66.67 ± 1.33	2.81 ± 0.05	6.4 ± 1.3
40k40k-SiO ₂	0.1	7.68 ± 0.54	93%	78.62 ± 0.70	3.32 ± 0.08	5.6 ± 0.8
	0.2	12.50 ± 0.76	98%	77.93 ± 0.22	2.94 ± 0.05	6.7 ± 0.3
	0.3	6.91 ± 1.59	97%	76.63 ± 2.05	3.02 ± 0.19	5.4 ± 1.9

Figure 9. Representative stress strain curves for (a) bare SiO_2 /epoxy nanocomposites; (b) 20k20k- SiO_2 /epoxy nanocomposites; and (c) 40k40k- SiO_2 /epoxy nanocomposites at different volumetric loadings of SiO_2 cores.

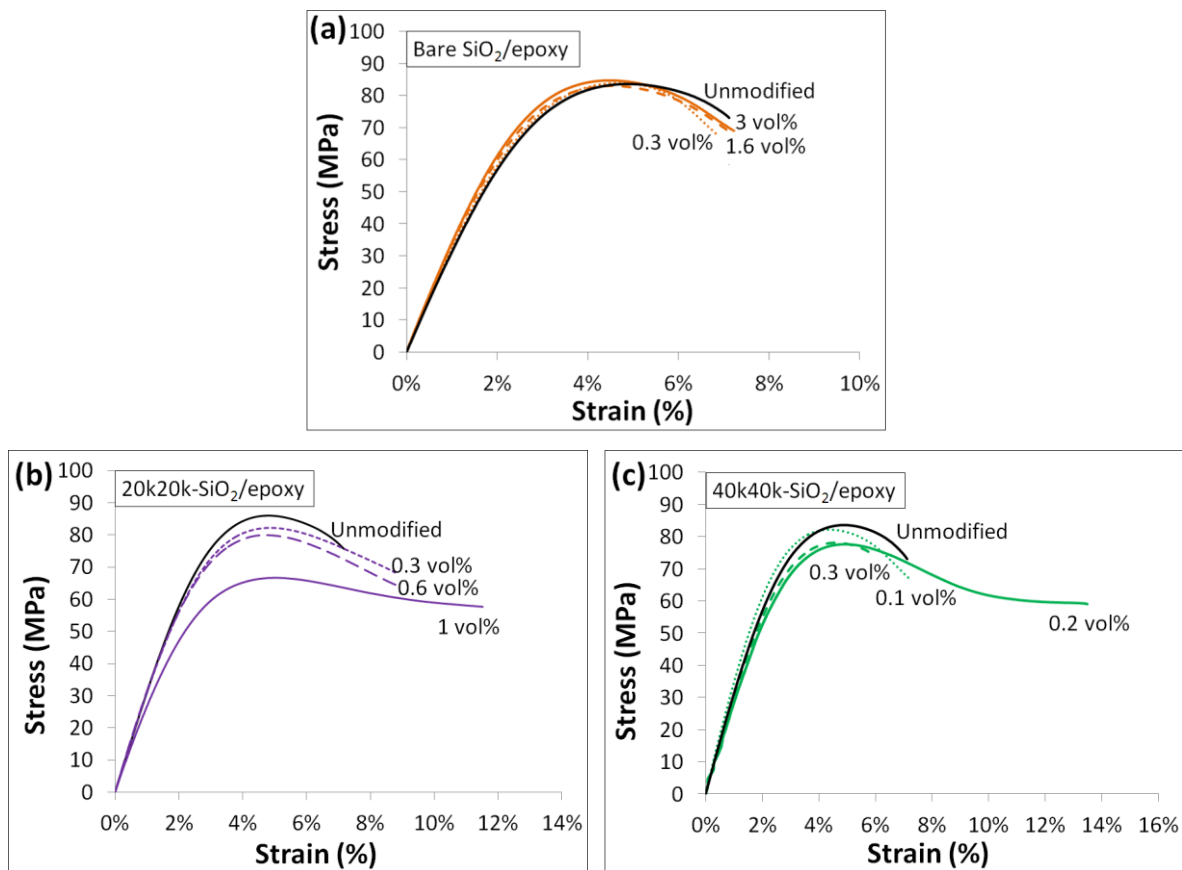
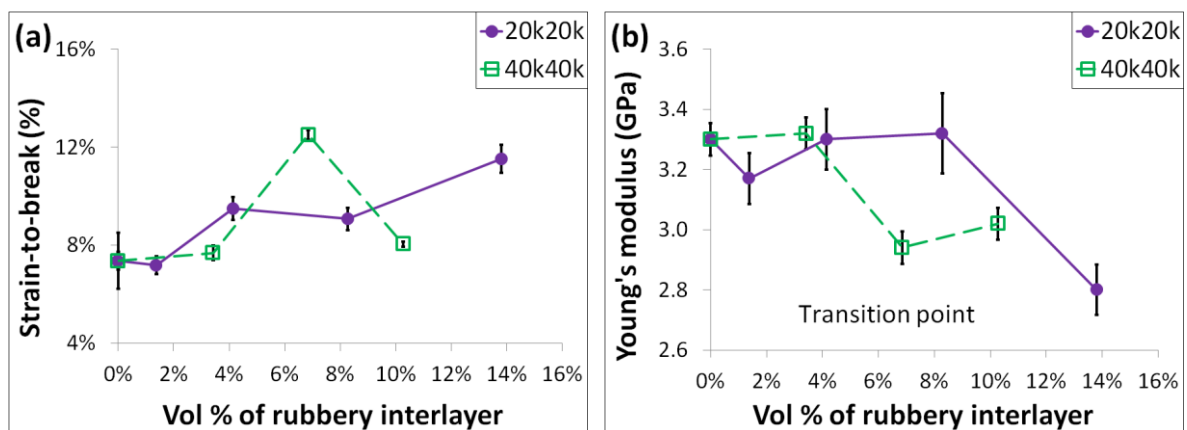
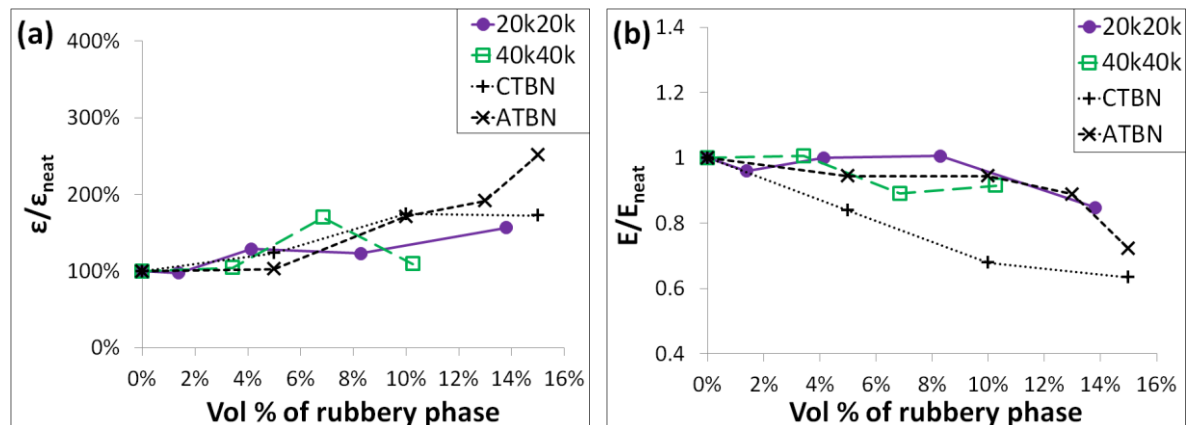


Figure 10. A plot of (a) strain-to-break; and (b) modulus vs. vol% of PHMA rubbery interlayer for the 20k20k and 40k40k systems.



A comparison of the normalized modulus and strain-to-break of the new rubbery copolymer grafted SiO_2 /epoxy nanocomposites to some conventional liquid rubber filled epoxy composites at similar testing conditions and with a similar matrix is shown in Figure 11. The grafted SiO_2 /epoxy nanocomposites exhibit a slightly larger extent of strain-to-break increase at low loadings of the rubbery phase than the conventional rubbers (see Figure 11(a)), but maintain the Young's modulus better than some conventional rubber fillers, especially for the 20k20k system.

Figure 11. (a) Comparison of the improvement in the strain-to-break vs. the volumetric loading of the rubbery phase between the rubbery copolymer grafted SiO_2 /epoxy nanocomposites and conventional rubber (CTBN and ATBN) filled epoxy composites; (b) Comparison of the Young's modulus vs. the volumetric loading of the rubbery phase between the rubbery copolymer grafted SiO_2 /epoxy nanocomposites and conventional rubber (CTBN and ATBN) filled epoxy composites [29].



3.4. Fracture Mechanisms

A brittle fracture surface usually consists of a mirror zone, mist zone and hackle zone [11]. The mirror zone is the slow crack propagation region next to the crack initiation site. It is usually smooth because the crack is propagating within a plane. As the crack starts to grow faster, a narrow mist zone is developed, where the crack is still propagating in the original crack growth plane. Right after the mist zone, cracks began to bifurcate into 3D planes, leading to a rough hackle zone [30]. The fracture surfaces of the neat epoxy, 20k20k- SiO_2 /epoxy at 0.3 and 1 vol% SiO_2 cores and 40k40k- SiO_2 /epoxy at 0.1 and 0.2 vol% SiO_2 cores after tensile failure are shown in Figures 12–14. The three zones are observed in all the materials. The mirror zones are marked in white circles on the overview SEM images in Figure 12.

Figure 12. Scanning Electron Micrographs showing the tensile fracture surfaces of (a) the neat epoxy; (b) 0.3 vol% 20k20k- SiO_2 nanocomposites; (c) 1 vol% 20k20k- SiO_2 nanocomposites; (d) 0.1 vol% 40k40k- SiO_2 nanocomposites; and (e) 0.2 vol% of 40k40k- SiO_2 nanocomposites. "A": mirror zone, "B": mist zone and "C": hackle zone.

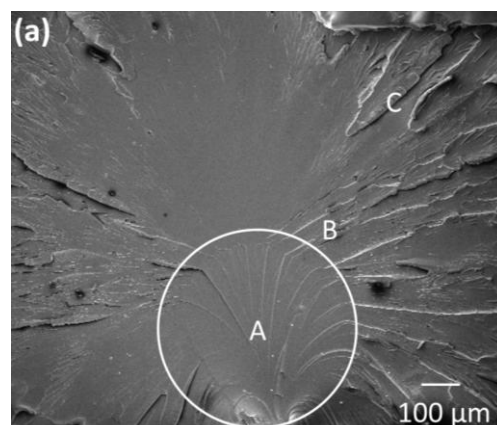
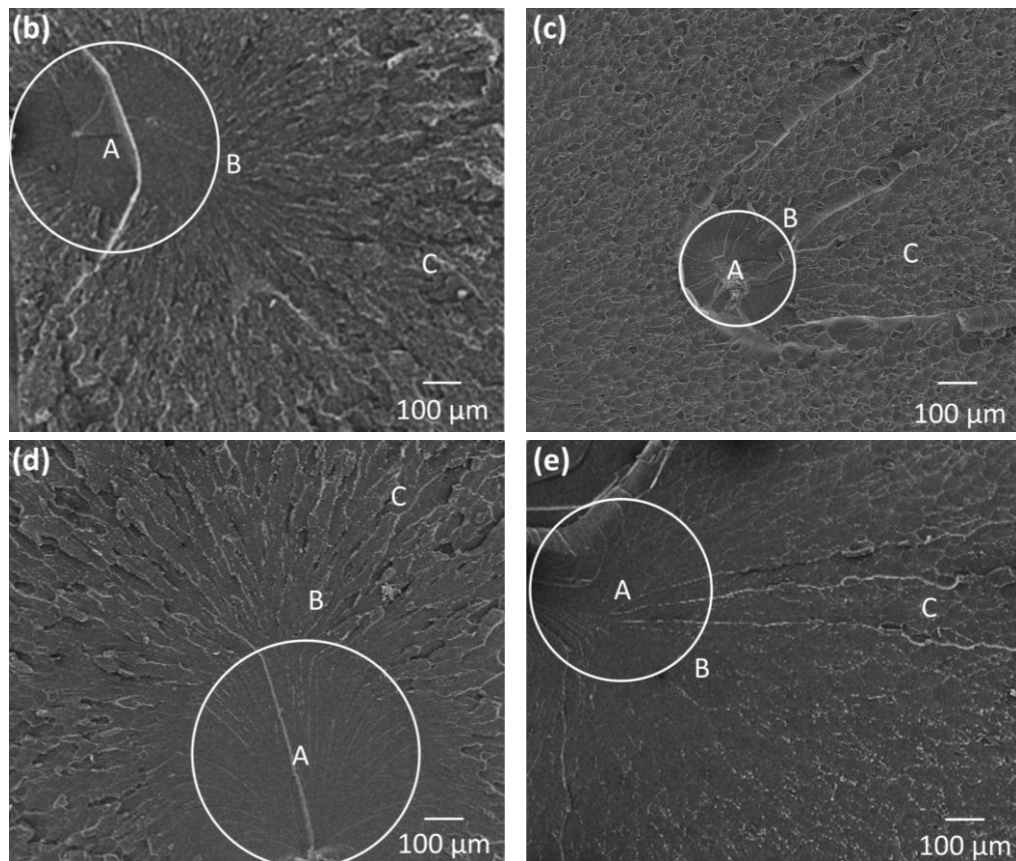


Figure 12. Cont.



Cavitation or plastic void growth of the rubber layer can be seen in the magnified mirror zones of the nanocomposites (see Figure 13(b–e)), which promotes plastic deformation in the matrix, hinders crack growth, and generates a rougher mirror zone surface. This leads to the improvement in ductility and toughness in the rubbery copolymer grafted SiO_2 nanoparticle composites as shown in Table 4 and Figures 9 and 10. Note that the 20 kg/mol PHMA and 40 kg/mol PHMA grafted rubbery interlayer exhibit cavitation or void growth (Figure 13(b–i)), which might result in similar extent of the improvement in ductility of the epoxy matrix at the same volume percent of the rubbery interlayer.

Figure 13. Scanning Electron Micrographs showing the ‘mirror’ zone on tensile fracture surfaces of (a) neat epoxy; (b), (d) 0.3 vol% of 20k20k- SiO_2 nanocomposites; (c), (e) 1 vol% of 20k20k- SiO_2 nanocomposites; (f), (h) 0.1 vol% 40k40k- SiO_2 nanocomposites; and (g), (i) 0.2 vol% of 40k40k- SiO_2 nanocomposites.

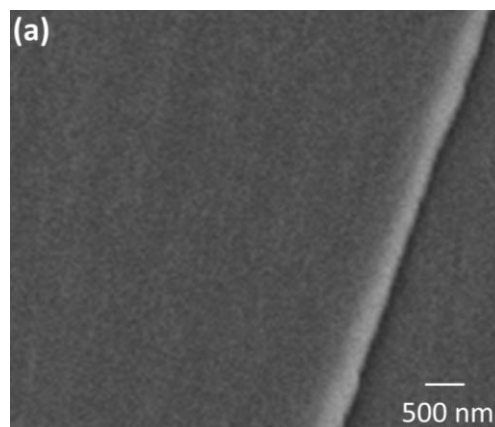


Figure 13. Cont.

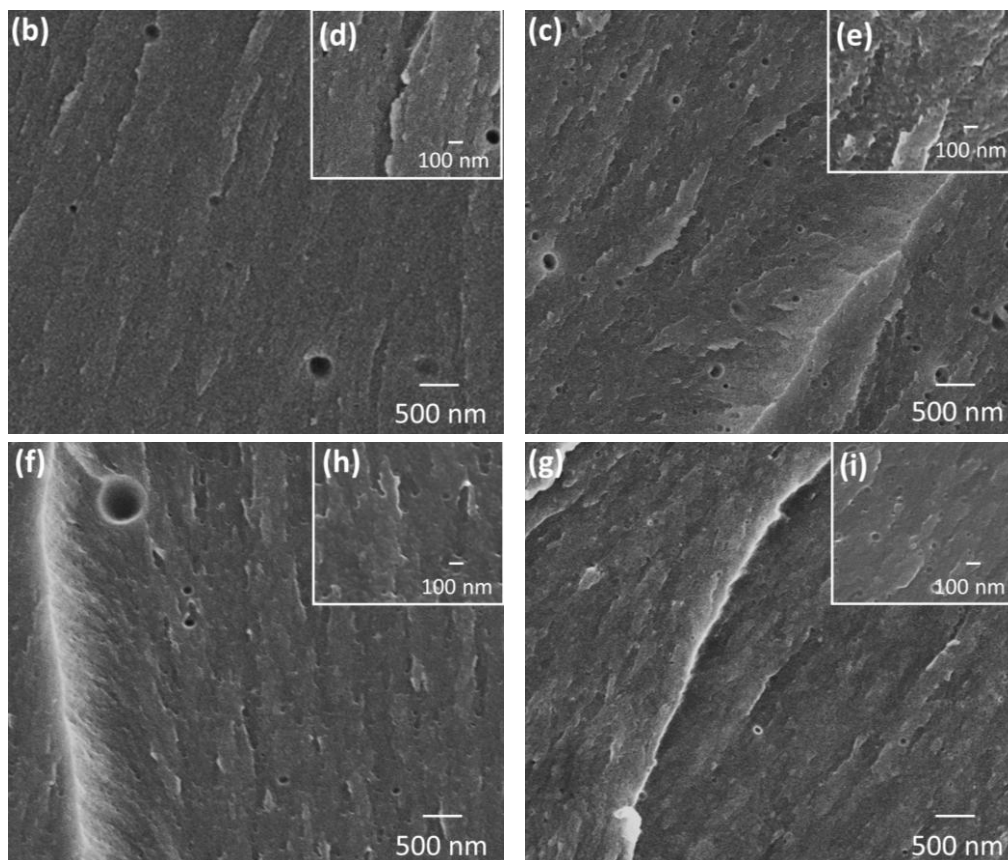


Figure 14. SEM images of the hackle zones of (a) the neat epoxy and the nanocomposites with (b) 0.3 vol% of 20k20k-SiO₂; (c) 1 vol% of 20k20k-SiO₂; (d) 0.1 vol% of 40k40k-SiO₂; (e) 0.2 vol% of 40k40k-SiO₂; (f) higher magnification for 1 vol% 20k20k; and (g) higher magnification for 0.2 vol% 40k40k.

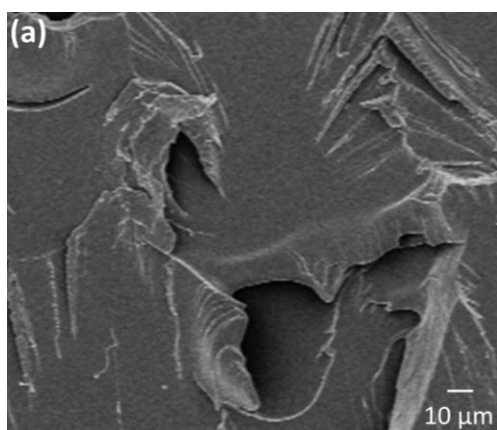
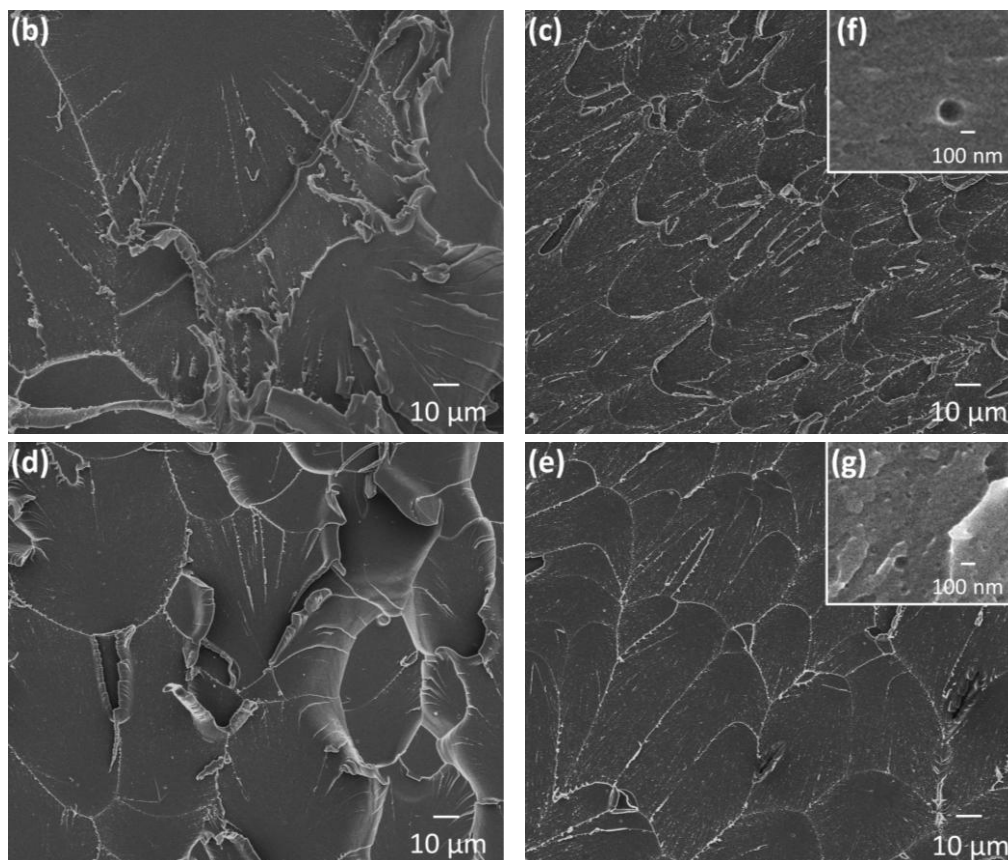


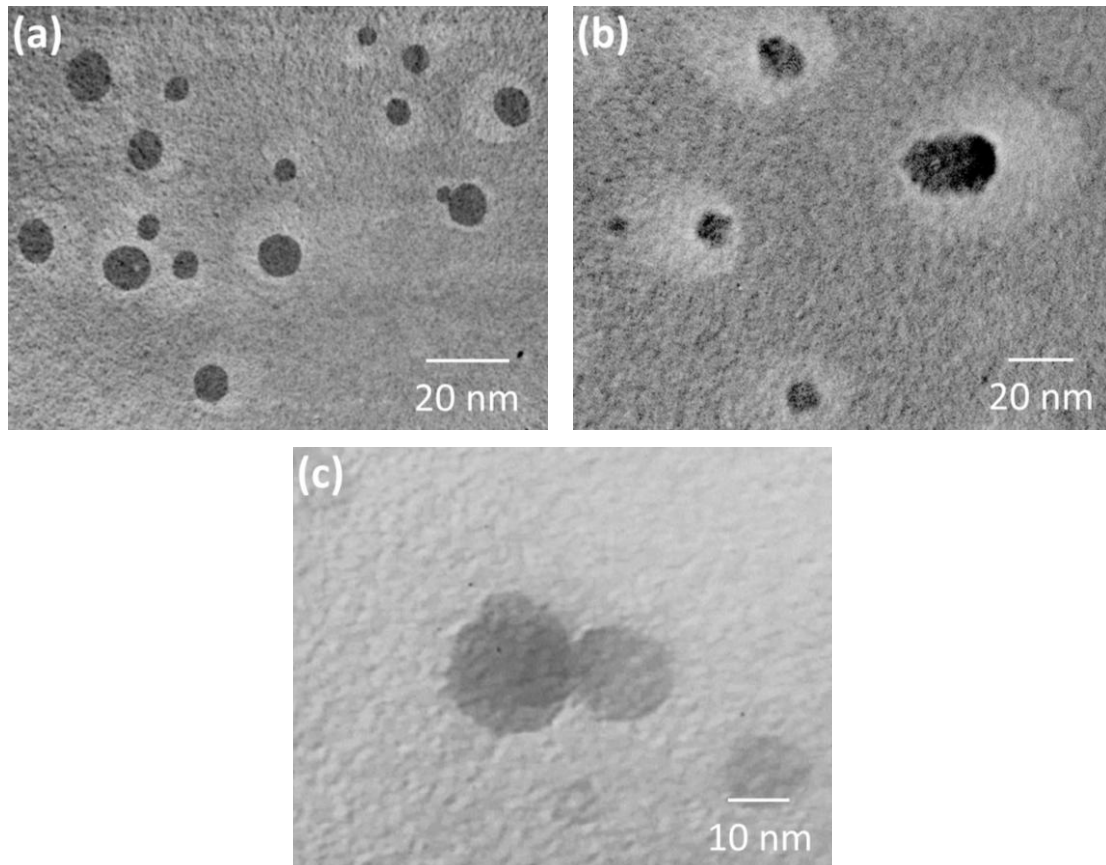
Figure 14. Cont.



The features in the hackle zone for the neat epoxy and low concentration copolymer grafted SiO_2 /epoxy nanocomposites (marked as region “C” in Figure 12 and shown in Figure 14) have random 3D features. This is because crack branching produces severe surface roughening; however, it doesn’t effectively retard crack growth [31]. Unlike the neat epoxy and the nanocomposites at low loadings, the 1 vol% 20k20k and 0.2 vol% 40k40k show features of parabolic patterned markings (see Figure 14(c,e)). The formation of the parabolic markings is believed to be a result of interaction between the crack front and the cavitation, which has also been observed in this region (see Figure 14(f,g)) [32]. This interaction might also contribute to the improvement of the ductility and tensile toughness of the epoxy nanocomposites at those loadings, as they achieved the most improvement compared to other loadings, which do not show the parabolic markings in the hackle zone (see Table 3).

To understand the leading mechanisms for the improvement of the mechanical properties of the epoxy matrix by the rubbery grafted SiO_2 nanoparticles, transmission electron microscopy (TEM) micrographs of thin slices of material perpendicular to the fracture surface were taken. The TEM micrographs of the fracture damage zone of the 1 vol% 20k20k nanocomposite and the 0.3 vol% 40k40k nanocomposites are shown in Figure 15. There are voids around the SiO_2 nanoparticles and it is caused by the rubbery interlayer cavitation and deformation. Similar images taken of non-deformed samples did not show the contrast exhibited here.

Figure 15. Transmission electron micrographs near the fracture surface of (a) 1 vol% 20k20k nanocomposites; (b) 0.3 vol% 40k40k nanocomposites; and (c) 1 vol% 20k20k as prepared.



The cavitation causes permanent failure in the rubbery interlayer, which results in energy release. The energy released by cavitation is negligible and does not contribute to the toughening directly but makes it easy for the matrix to deform plastically, as proven by Bagheri and Pearson *et al.* who found that the toughening efficiency is similar for rubbers with different cavitation resistance and pre-formed voids, which did not involve any cavitation energy [33]. Rubber cavitation, however, is usually followed by plastic void growth extending to the matrix and local shear yielding [34], both of which are believed to be primary toughening mechanisms in rubber filled epoxy. The irreversible plastic void-growth in the matrix dissipates energy and contributes to the enhanced fracture energy, and the local shear yielding can promote plastic deformation in the matrix, which also improves the fracture energy [35].

There are well-established models from Huang and Kinloch predicting the contribution of plastic void growth and shear banding to the fracture energy in a process zone at the tip of a pre-crack under plane strain uniaxial tension [38]. In this study, we have tested the tensile properties and thus the model cannot be used directly. Because energy density is an intensive property, which is independent of volume of the process zone, the dissipated strain-energy density instead of the fracture energy of the tensile fracture is theoretically calculated to compare to the measured tensile strain-energy density. The dissipated strain-energy density (U_v) for a void in the epoxy to undergo plastic void growth was quantitatively studied by Huang and Kinloch [38] and is expressed as:

$$U_v = p(f_v - f_r) \quad (11)$$

where p is the local hydrostatic stress, and f_v and f_r are the volumetric loading of the voids and rubbery interlayer. Since f_v and f_r of the current studied system can be measured and calculated, the only unknown parameter is the local hydrostatic stress, which is different from that in the process zone at a crack tip as given by Huang and Kinloch [38]. Once necking has occurred in a specimen under a uniaxial plane strain tensile test, there is a triaxial stress state in the onset region of the neck [36–38]. When the neck profile is concave is there a hydrostatic stress state. The hydrostatic stress at the concave profile region in the uniaxial tension can be calculated from the following equations [40–42]:

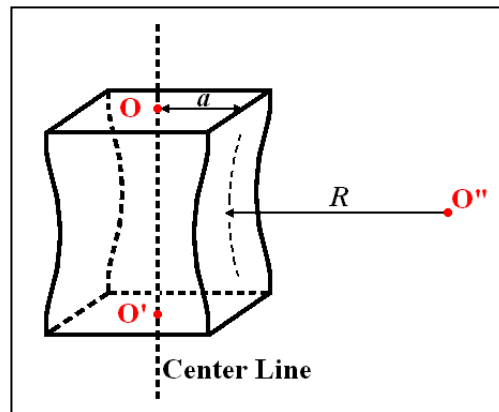
$$p = \sigma_{yt} \left(\frac{1}{F_T} - 1 \right) \quad (12)$$

$$F_T = \frac{1}{\left(1 + \frac{2R}{a}\right) \cdot \ln\left(1 + \frac{a}{2R}\right)} \quad (13)$$

$$\frac{a}{R} = 3.2 \left[1 - e^{\frac{-(\varepsilon_b - \varepsilon_n)}{3}} \right] \quad (14)$$

where σ_{yt} is the yield stress of the material; F_T is the local triaxiality factor; a/R is the ratio of half of the cross-section edge a to the profile radius R of the neck as shown in Figure 16. There is an empirical relationship [42] between a/R and ε_b and ε_n which are the strain at break and the strain at the onset of necking, respectively. ε_b and ε_n were determined experimentally.

Figure 16. Neck region of a tensile bar.



The strain energy density of a tensile test can be calculated as the area underneath the stress strain curve (Equation (15)), which is also known as the tensile toughness:

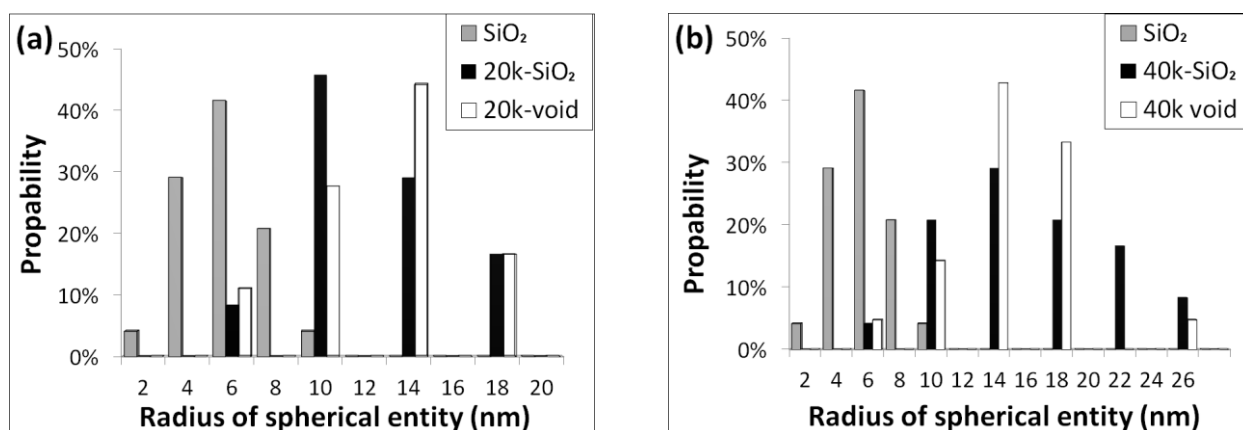
$$W = \int_0^{\varepsilon_b} \sigma \cdot d\varepsilon \quad (15)$$

where ε_b is the strain-to-break; σ and ε are stress and strain of a tensile curve; and W is the strain energy density (or tensile toughness). The difference in the tensile toughness of the composites and the epoxy matrix is equal to the strain energy density contribution from all operating toughening mechanisms. Since the plastic void growth mechanism is obviously happening as shown in Figure 15, the following equation holds

$$W_c - W_u = \Delta W = U_v + \sum U_{1,2 \dots n} \quad (16)$$

where the subscript c and u mean the composite and unmodified epoxy; and U_v is the strain energy density contributed by plastic void growth. The sum is the sum of the strain energy contribution by other operating mechanisms.

Figure 17. (a) Distribution of SiO₂ core size, 20 kg/mol PHMA-SiO₂ and void surrounded SiO₂ in 20k20k systems; (b) Distribution of SiO₂ core size, 40 kg/mol PHMA-SiO₂ and void surrounding SiO₂ in 40k40k systems.



Characterization of the deformation due to plastic void growth and the size distribution of SiO₂ nanoparticles were measured from 5 TEM micrographs and are summarized in Figure 17. The distribution of rubbery layer thickness is given in Figure 4. The distribution of the void sizes of both systems is overlapping; however the weighted mean of the void size in both systems shows that the voids are slightly bigger than the rubbery interlayer size as summarized in Table 6. The volume difference between the void and the rubbery layer was used to calculate the plastic void growth contribution to the tensile toughness.

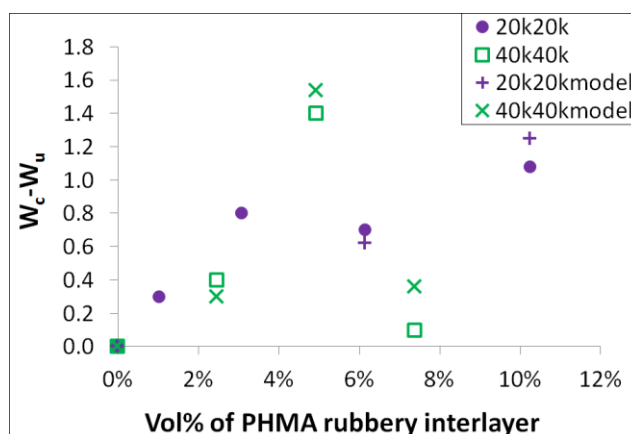
Table 6. Weighted mean of rubbery interlayer size and void size in both 20k20k and 40k40k systems.

	vol% of SiO ₂ Cores	Weight Mean of Rubbery Interlayer Thickness (nm)	vol% of Rubbery Interlayer	Weight Mean of Void Size from the Surface of the SiO ₂ to the Edge of the Void	vol% of Void
20k20k	0.1%	6.33	1.03%	6.83	Not measured yet
	0.3%		3.08%		Not measured yet
	0.6%		6.16%		6.98%
	1.0%		10.26%		11.63%
40k40k	0.1%	10.16	2.46%	11.47	3.07%
	0.2%		4.93%		6.13%
	0.3%		7.39%		9.20%

By substituting the volume increase that occurs after rubbery interlayer cavitation in Equations (11) and (16), the fracture mechanism involving plastic void growth is compared with the experimental data of both systems in Figure 18. There is a good match between the theoretical model and experimental

data for the 40k40k system of all three tested loadings and the 20k20k system above 4 vol% of the rubbery interlayer. The plastic void growth was not yet measured for the 20k20k system at low loadings, so no comparison is made. From this analysis, the plastic void growth mechanism is believed to be the leading mechanism for improving the tensile toughness in the studied copolymer grafted SiO_2 /epoxy nanocomposites.

Figure 18. Plastic void growth mechanism in rubbery interlayer grafted SiO_2 /epoxy.



Localized shear yielding [39–42] is another possible phenomenon following rubbery interlayer cavitation. Localized shear yielding will decrease the composites yield strength. The tensile results in Table 4 show that the yield strength decreases as the rubbery interlayer volume percent increases. In addition, the voids around the SiO_2 nanoparticles in both 20k20k and 40k40k systems shown in Figure 15 are elliptical although not oriented. However, the shear bands were not visible in a TEM, and thus the contribution from shear banding is unclear.

Other fracture mechanisms such as crack bridging and pinning [43] and crack deflection [44,45] might also be operating. Crack bridging is unlikely due to the small dimensions of the rubbery layer. Crack pinning is a possible mechanism, since the crack might propagate at slower velocity when it meets the plastic void growth region around the SiO_2 nanoparticles. However there is no clear crack pinning feature on the fracture surface of the nanocomposites in Figures 12–14, indicating the region of plastic deformation around the SiO_2 nanoparticles might not be big enough to launch this mechanism. Wetzel *et al.* [46] found that crack deflection increases with increasing content of rigid nanoparticles. However, in the current study, the volume percent of the SiO_2 cores is less than 1 vol%, which is unlikely to cause significant crack deflection. At such low particle volume percent, Wetzel *et al.* observed a large discrepancy between the crack deflection model and experimental data for 13 nm Al_2O_3 nanoparticle filled epoxy. Therefore, the energy release by crack deflection is probably negligible in the current study.

4. Summary

Copolymer grafted SiO_2 nanoparticles with a rubbery PHMA inner layer and a matrix compatible PGMA outer layer were prepared by RAFT polymerization and were found to disperse well in an epoxy matrix. The rubbery layer thickness can be tailored by varying the molecular weight of the rubbery block. An improvement of the strain-to-break was found to be proportional to the volume

percent of the rubbery interlayer. Both the 20 kg/mol and the 40 kg/mol PHMA rubbery interlayer are thick enough to cavitate and cause plastic void growth. The plastic void growth model fit the data reasonably well indicating that the mechanism is operating. Shear banding might also be occurring, but was not visible. Other common toughening mechanisms such as crack bridging, crack pinning and crack deflection are not likely to operate in the studied systems. Though the modulus and tensile strength of the composites decreased with the addition of the rubbery polymer grafted SiO₂, they are somewhat better than for rubber filled epoxy composites. Thinner rubbery layers lead to equivalent improvements of strain to failure, but less of a reduction in Young's modulus of the composites.

Acknowledgments

This work was supported by ABB Corporate Research and Swedish Research Council (IFA 2007-5095). It is also supported by the Nanoscale Science and Engineering Initiative of the National Science Foundation under NSF Award Number DMR-0117792.

References

1. Lee, H.; Neville, K. *Handbook of Epoxy Resins*, 1st ed.; McGraw-Hill: New York, NY, USA, 1967.
2. Kunz-Douglass, S.; Beaumont, P.W.R.; Ashby, M.F. A model for the toughness of epoxy-rubber particulate composites. *J. Mater. Sci.* **1980**, *15*, 1109–1123.
3. Kunz, S.C.; Sayre, J.A.; Assink, R.A. Morphology and toughness characterization of epoxy resins modified with amine and carboxyl terminated rubbers. *Polymer* **1982**, *23*, 1897–1906.
4. Hwang, J.F.; Manson, J.A.; Hertzberg, R.W.; Miller, G.A.; Sperling, J.H. Structure-property relationships in rubber-toughened epoxies. *Polym. Eng. Sci.* **1989**, *29*, 1466–1476.
5. Qian, J.Y.; Pearson, R.A.; Dimonie, V.L.; Ei-Aasser, M.S. Synthesis and application of core-shell particles as toughening agents for epoxies. *J. Appl. Polym. Sci.* **1995**, *88*, 439–448.
6. Lovell, P.A.; McDonald, J.; Saunders, D.E.J.; Young, R.J. Studies of rubber-toughened poly(methyl methacrylate): 1. Preparation and thermal properties of blends of poly (methyl methacrylate) with multiple-layer toughening particles. *Polymer* **1993**, *34*, 61–69.
7. Day, R.J.; Lovell, P.A.; Wazzan, A.A. Toughened carbon/epoxy composites made by using core/shell particles. *Compos. Sci. Technol.* **2001**, *61*, 41–56.
8. Johnsen, B.B.; Kinloch, A.J. Toughening mechanisms of nanoparticle-modified epoxy polymers. *Polymer* **2007**, *48*, 530–541.
9. Balakrishnan, S.; Start, P.R.; Raghavan, D.; Hudson, S.D. The influence of clay and elastomer concentration on the morphology and fracture energy of preformed acrylic rubber dispersed clay filled epoxy nanocomposites. *Polymer* **2005**, *46*, 11255–11262.
10. Wetzel, B.; Hauptert, F.; Zhang, M.Q. Epoxy nanocomposites with high mechanical and tribological performance. *Compos. Sci. Technol.* **2003**, *63*, 2055–2067.
11. Zhao, S.; Schadler, L.S.; Hillborg, H.; Auletta, T. Improvements and mechanisms of fracture and fatigue properties of well-dispersed alumina/epoxy nanocomposites. *Compos. Sci. Technol.* **2008**, *68*, 2976–2982.
12. Lan, T.; Pinnavaia, T.J. Clay-reinforced epoxy nanocomposites. *Chem. Mater.* **1994**, *6*, 2216–2219.

13. Allaoui, A.; Bai, S.; Cheng, H.M.; Bai, J.B. Mechanical and electrical properties of a MWNT/epoxy composite. *Compos. Sci. Technol.* **2002**, *62*, 1993–1998.
14. Rafiee, M.A.; Rafiee, J.; Zhou, W.; Song, H.H.; Yu, Z.Z.; Koratkar, N. Enhanced mechanical properties of nanocomposites at low graphene content. *ACS Nano* **2009**, *3*, 3884–3890.
15. Kinloch, A.J.; Mohammed, R.D.; Taylor, A.C.; Eger, C.; Spenger, S.; Egan, D. The effect of silica nano particles and rubber particles on the toughness of multiphase thermosetting epoxy polymers. *J. Mater. Sci.* **2005**, *40*, 5083–5086.
16. Liang, Y.L.; Pearson, R.A. The toughening mechanism in hybrid epoxy-silica-rubber nanocomposites (HESRN). *Polymer* **2010**, *51*, 4880–4890.
17. Lee, J.; Yee, A.F. Effect of rubber interlayers on the fracture of glass bead/epoxy composites. *J. Mater. Sci.* **2001**, *36*, 7–20.
18. Li, C.Z.; Han, J.W.; Ryu, C.Y.; Benicewicz, B.C. A versatile method to prepare RAFT agent anchored substrates and the preparation of PMMA grafted nanoparticles. *Macromolecules* **2006**, *39*, 3175–3183.
19. Li, C.Z.; Benicewicz, B.C. Synthesis of well-defined polymer brushes grafted onto silica nanoparticles via surface reversible addition-fragmentation chain transfer polymerization. *Macromolecules* **2005**, *38*, 5929–5936.
20. Rasband, W.S. *ImageJ*; US National Institutes of Health: Bethesda, MD, USA, 1997–2011. Available online: <http://imagej.nih.gov/ij/> (accessed on 19 October 2011).
21. Kissinger, H.E. Reaction kinetics in differential thermal analysis. *Anal. Chem.* **1957**, *29*, 1702–1706.
22. Ton-That, M.T.; Ngo, T.D.; Ding, P.; Fang, G.; Cole, K.C.; Hoa, S.V. Epoxy nanocomposites: Analysis and kinetics of cure. *Polym. Eng. Sci.* **2004**, *44*, 1132–1141.
23. Montserrat, S.; Flaque, C.; Calafell, M.; Andreu, G.; Malek, J. Influence of the accelerator concentration on the curing reaction of an epoxy-anhydride system. *Thermochim. Acta* **1995**, *213*, 269–270.
24. Guerrero, P.; De la Caba, K.; Vales, A.; Corcuera, M.A.; Mondragon, I. Influence of cure schedule and stoichiometry on the dynamic mechanical behavior of tetrafunctional epoxy resins cured with anhydrides. *Polymer* **1996**, *37*, 2195–2200.
25. Beiner, M.; Kahle, S.; Hempel, E.; Schroter, K.; Donth, E. Crossover region of dynamic glass transition in poly (n-hexyl methacrylate) by heat capacity spectroscopy. *Macromolecules* **1998**, *31*, 8973–8980.
26. Child, W.C., Jr; Ferry, J.D. Dynamic mechanical properties of poly-*n*-hexyl methacrylate. *J. Colloid Sci.* **1957**, *12*, 389–399.
27. Thompson, Z.J.; Hillmyer, M.A.; Liu, J.; Sue, H.J.; Dettloff, M.; Bates, F.S. Block copolymer toughened epoxy: Role of cross-link density. *Macromolecules* **2009**, *42*, 2333–2335.
28. Van der Sanden, M.C.M.; Meijer, H.E.H. Deformation and toughness of polymeric systems: 3. Influence of crosslink density. *Polymer* **1993**, *34*, 5063–5072.
29. Chikhi, N.; Fellahi, S.; Bakar, M. Modification of epoxy resin using reactive liquid (ATBN) rubber. *Eur. Polym. J* **2002**, *38*, 251–254.
30. Hull, D. *Fractography—Observing, Measuring and Interpreting Fracture Surface Topography*, 1st ed.; Cambridge University Press: Cambridge, UK, 1999; pp. 121–150.

31. Lawn, B. *Fracture of Brittle Solids*, 2nd ed.; Cambridge University Press: Cambridge, UK, 1993; p. 95.
32. Fineberg, J.; Marder, H.M. Instability in dynamic fracture. *Phys. Rep.* **1999**, *313*, 1–108.
33. Bagheri, R.; Pearson, R.A. Role of particle cavitation in rubber-toughened epoxies: 1. Microvoid toughening. *Polymer* **1996**, *17*, 4529–4538.
34. Huang, Y.; Kinloch, A.J. The role of plastic void growth in the fracture of rubber-toughened epoxy polymers. *J. Mater. Sci. Lett.* **1992**, *11*, 484–487.
35. Ma, J. Study of epoxy toughened by *in situ* formed rubber nanoparticles. *J. Appl. Polym. Sci.* **2008**, *110*, 304–312.
36. Nicolaou, P.D.; Semiatin, S.L. The effect of stress triaxiality on tensile behavior of cavitating specimens. *J. Mater. Sci.* **2001**, *36*, 5155–5159.
37. Lombard, C.M.; Goetz, R.L.; Semiatin, S.L. Numerical analysis of the hot tension test. *Metall. Trans. A* **1993**, *24A*, 2039–2047.
38. Ragab, A.R. Prediction of ductile fracture in axisymmetric tension by void coalescence. *Int. J. Fract.* **2000**, *105*, 391–409.
39. Kinloch, A.J. Relationship between the microstructure and fracture behavior of rubber-toughened thermosetting polymers. In *Rubber-Toughened Plastics*; Riew, C.K., Ed.; American Chemical Society: Washington, DC, USA, 1989; Volume 222, pp. 67–91.
40. Pearson, R.A.; Yee, A.F. Toughening mechanisms in elastomer-modified epoxies. *J. Mater. Sci.* **1986**, *21*, 2462–2474.
41. Bagheri, R.; Pearson, R.A. Role of particle cavitation in rubber-toughened epoxies. *Polymer* **1996**, *17*, 4529–4538.
42. Yee, A.F.; Li, D.M.; Li, X.W. The importance of constraint relief caused by rubber cavitation in the toughening of epoxy. *J. Mater. Sci.* **1993**, *28*, 6392–6398.
43. Kunz, S. A model for the toughness of epoxy-rubber particulate composites. *J. Mater. Sci.* **1980**, *15*, 1109–1123.
44. Faber, K.T.; Evans, A.G. Crack deflection process—I. Theory. *Acta Metall.* **1983**, *31*, 565–576.
45. Faber, K.T.; Evans, A.G. Crack deflection process—II. Experiment. *Acta Metall.* **1983**, *31*, 577–584.
46. Wetzels, B.; Rosso, P.; Hauptert, F.; Friedrich, K. Epoxy nanocomposites—Fracture and toughening mechanisms. *Eng. Fract. Mech.* **2006**, *73*, 2375–2398.